ScienceDirect

Acta Materialia
Volume 234, 1 August 2022, 118021

Rare-earth-free noncollinear metallic ferrimagnets $Mn_{4-x}Z_xN$ with compensation at room temperature

Rui Zhang [a], Yangkun He [a], Daniel Fruchart [b], J.M.D. Coey [a], Zsolt Gercsi [a]

Show more

Outline | Share Cite

https://doi.org/10.1016/j.actamat.2022.118021 Get rights and content

Abstract

Compensated ferrimagnets show no net magnetization like antiferromagnets, but their transport and magneto-optic properties resemble those of ferromagnets, thereby creating opportunities for applications in high-frequency spintronics and low energy loss communications. Here we study the modification of the noncollinear triangular ferrimagnetic spin structure of Mn_4N by a variety of metallic substitutions Z (Z = Cu — Ge and Ag — Sn) to achieve compensation at room temperature. The noncollinear frustrated $2.35\mu_B$ moments of Mn on 3*c* sites of the (111) kagome planes tilt about 20° out-of-plane in Mn_4N and are easily influenced by the substitutions on 1*a* sites, leading to an efficiency of compensation in $Mn_{4-x}Z_xN$ that increases gradually from group 11 (Cu, Ag) to group 14 (Ge, Sn) with increasing number of valence electrons. Elements from the 5th period are more efficient for compensation than those from the 4th period due to lattice expansion. The manganese site moments analyzed by constrained density functional theory are determined by Z, orbital hybridization, charge transfer and the tilt angle. The Ga compound with compensation at room temperature for $x \approx 0.26$ is recommended for high-frequency spintronic applications.

Graphical abstract

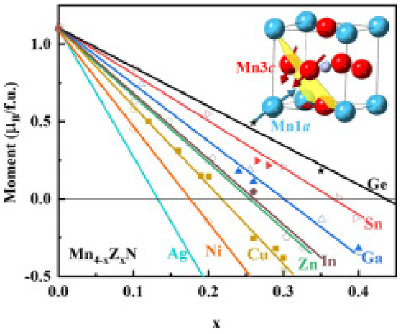

Download : Download high-res image (191KB) Download : Download full-size image

Previous Next

Keywords

Metallic perovskites; Noncollinear magnetic structure; Kagome lattice; Ferrimagnetism; Compensation temperature; Mn_4N

---

1. Introduction

Low energy-loss communications and high-frequency spintronic applications could benefit from magnetic materials with a small net magnetic moment at room temperature [1]. Although antiferromagnetic (AFM) materials have no net moment, apart from some exceptions with special symmetry [2,3], they usually lack net spin polarization and do not exhibit transport properties such as the anomalous Hall effect. Ferrimagnetic (FiM) metals exhibit transport properties just like ferromagnets, while their magnetization can also fall to zero if the net moments of the antiparallel sublattices compensate, leading to the current interest in developing new compensated ferrimagnets for spintronics [4,5].

Ferrimagnets usually consist of two sublattices with different magnetic moments where AFM intersublattice exchange may coexist with ferromagnetic (FM) interactions. The most common type, collinear ferrimagnetism, is shown in Fig. 1a; well-studied examples are Fe_3O_4, $Y_3Fe_5O_{12}$, amorphous Gd-Co [6] and Mn_2Sb [7]. In these materials, the moments within each sub-lattice are aligned parallel while the two sublattices are antiparallel. A less common non-collinear ferrimagnetic (ncFiM) magnetic structure is shown in Fig. 1b, where the coupling is between a non-collinear antiferromagnetic sublattice, and a ferromagnetic sublattice. The significant difference in the second type is that the ferrimagnetism is non-collinear. Examples include $Ni(NO_3)_2$ [8], $MnCr_2O_4$ [9] and $Ho_2Fe_{14}B$ [10] at low temperature. Unlike oxides, which are usually insulating, metallic ferrimagnets are often Mn-based or else R-T-based, where R is a heavy rare-earth and T is Fe or Co. The former category avoids the use of rare-earth metals and the Curie temperature is often high, which it is well suited for applications.

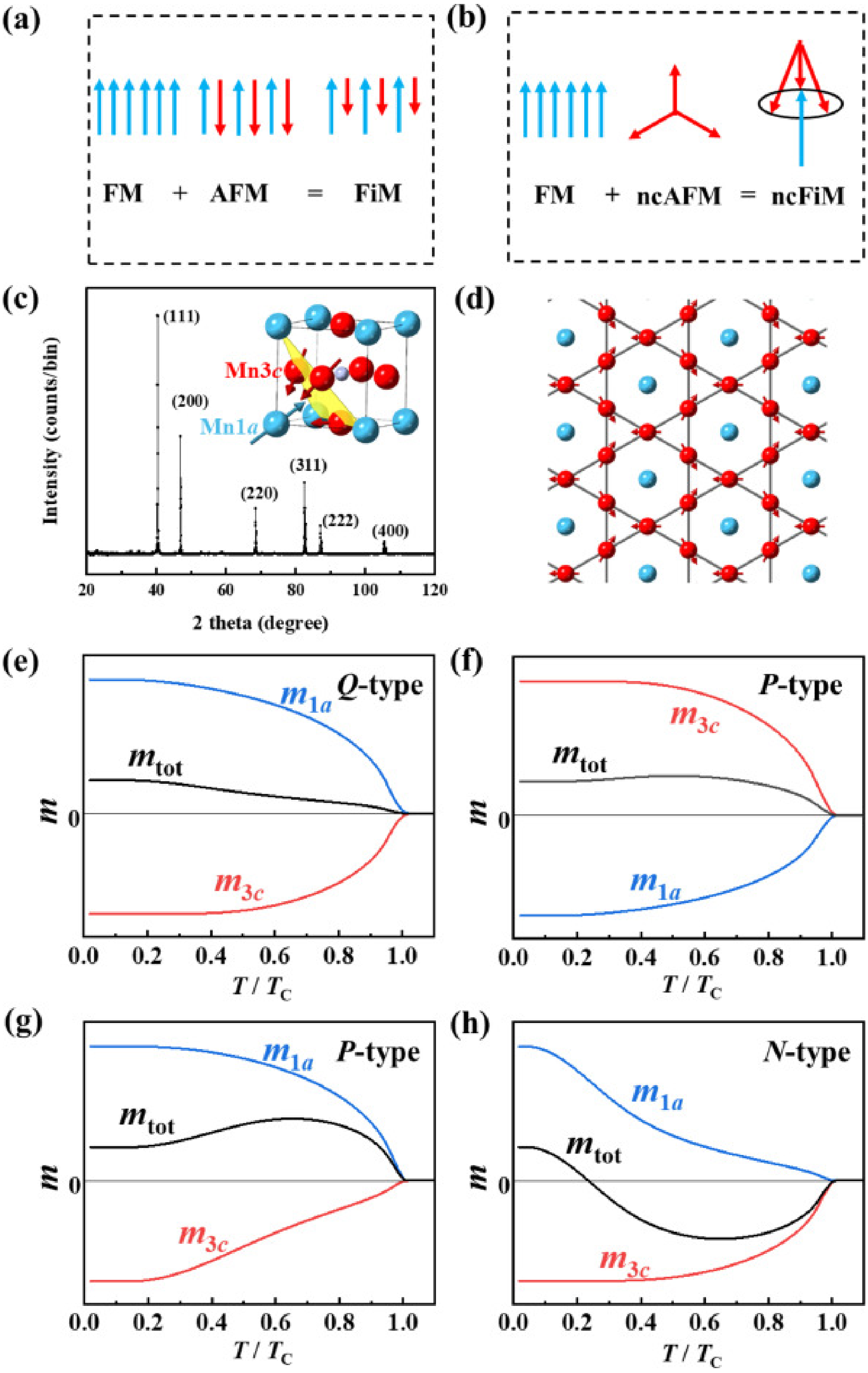

Fig. 1. Ferrimagnetic prototypes. (a) A collinear ferrimagnetic (FiM) spin structure is a combination of ferromagnetic (FM) and antiferromagnetic (AFM) spin structures. (b) The noncollinear ferrimagnetic (ncFiM) structure combines non-collinear antiferromagnetic (ncAFM) and FM structures. (c) XRD pattern of Mn_4N. The inset shows crystal and magnetic structure with Γ^{4g} triangular ferrimagnetism in the (111) plane. Grey, blue and red atoms represent N, Mn^{1a} and Mn^{3c}, respectively. (d) Kagome lattice of Mn^{3c} in a (111) plane showing the Γ^{4g} magnetic structure. The out-of-plane magnetic component is not shown. Three types of temperature-dependent magnetization curves are shown schematically for a ferrimagnet with two sublattices (1a and 3c for Mn_4N) in panels (e)-(h). (e) is for $m_{1a} > 3m_{3c}$ with n_{1a3c} as the main molecular field coefficient; (f) is for $m_{1a} < 3m_{3c}$ with n_{1a3c} as the main molecular field coefficient; (g) is for $m_{1a} > 3m_{3c}$ with n_{1a1a} as the main molecular field coefficient and (h) $m_{1a} > 3m_{3c}$ and n_{3c3c} as the main molecular field coefficient. A collinear model is used here. In a triangular model the chief difference in the shape of the curve is

the non-zero slope at low temperatures (see Fig. 2a). (For interpretation of the references to colour in this figure legend, the reader is referred to the web version of this article.)

The interstitial compound Mn_4N crystallizes in the space group $Pm\bar{3}m$ where N atoms occupying the body-centered interstitial site are coordinated by an octahedron of six Mn atoms in the 3*c* face-center positions, as shown in Fig. 1c. The Mn in the 1*a* corner positions is not in direct contact with the nitrogen. The magnetic order has been investigated both experimentally and theoretically. Initially, the compound was thought to have a collinear ferrimagnetic structure with moments lying along [111] [11,12] with a large 1*a* site magnetic moment $m_{1a} = 3.8\ \mu_B$ and a 3*c* site moment $m_{3c} = 0.9\ \mu_B$ that was much-reduced by *p*-*d* hybridization with the neighboring nitrogen [12]. Subsequent neutron diffraction with polarization analysis revealed that triangles of 3*c* atoms in (111) planes, where they from a kagome lattice shown in Fig. 1d, add a 120° triangular antiferromagnetic component to the 3*c* sublattice spin structure, where the axes of the spin components in the (111) plane either either meet at the centre of the triangle (Γ^{4g} mode) or else lie along the sides of the triangle (Γ^{5g} mode). Only a small anisotropy energy separates the two solutions, and the modes may coexist at finite temperature [13]. Calculations by Uhl et al. [14] confirmed the noncollinear 'umbrella' structure with the net sublattice moments aligned antiparallel along a [111] axis, producing a net moment close to the value of 1.1 μ_B that is found experimentally [12]. The Γ^{4g} mode has a topological character that accounts for the large anomalous Hall effect in many $Mn_{4-x}Z_xN$ materials [15]. The assumption that Mn_4N is a collinear ferrimagnet is therefore unwarranted and may lead to misleading conclusions [16].

In the Weiss mean-field model the temperature-dependent magnetization (*M*-*T*) curves for ferrimagnets can be categorized into three types depending on the moments and the molecular field coefficients within and between sublattices (n_{1a1a}, n_{1a3c} and n_{3c3c}) [17]; some curves are shown in Figs. 1e-1h. The *M*-*T* curve of binary Mn_4N [18,19] is *Q*-type, without compensation, where the magnetization of the 1*a* sublattice is larger than that of the 3*c* sublattice at all temperatures and n_{1a3c} is the main molecular field coefficient. An *N*-type *M*-*T* curve with compensation may be achieved by partial substitution of Z for Mn on 1*a* sites in $Mn_{4-x}Z_xN$ (Z = Co, Ni, Cu, Zn, Ga, Ge, As, Rh, Pd, Ag, Cd, In, Sn, Sb, Pt, Au and Hg with $x < 1$) [20,21]. All these substitutions are expected to produce compensation in the ordered $Mn_{4-x}Z_xN$ alloys, and some have been identified experimentally [22], [23], [24], [25]. Complete substitution x = 1 gives a metallic perovskite structure Mn_3ZN. Though most dopants are nonmagnetic, it is found that compensation is achieved at quite different values of *x* for different elements [26]. Therefore, it is necessary to analyze the doping efficiency in order to clarify the governing physical mechanisms that allow us to productively design novel Mn_4N-based compensated ferrimagnets for room temperature applications.

In this study, we first reveal the origin of the noncollinear ferrimagnetism of Mn_4N. We then demonstrate compensation at room temperature with various non-magnetic alloying elements and compare their efficiency. We discuss the findings in relation to valance electron count, magnetic moment, tilt angle and lattice constant, based on experimental data and constrained density functional theory calculations.

2. Methods

High purity (> 99.99%) elements of Mn and Z = Cu, Ga, Ge, In, Sn were arc-melted together five times to prepare homogeneous polycrystalline ingots. Extra Mn (2%) was added to compensate loss due to its high vapor pressure. The ingots were then ground into powder and reacted with N_2 (> 99.99%) at 750 – 800 °C at a pressure of 50 kPa for 1 day. We found that if the N_2 pressure is too large (100 kPa) a Mn_2N impurity phase will form in some samples with small values of *x*. Nitrogen deficiency can lead nitrogen vacancies or formation of γ- or β-Mn type impurities. Additional heat treatment (annealing at 660 °C in vacuum for one day was needed for Mn-Cu and Mn-Ge ingots before grinding them into powder to transform γ-Mn into β-Mn, owing to the ductile mechanical properties of γ-Mn which makes it difficult to grind.

The composition of the polycrystalline samples was checked by energy-dispersive X-ray spectroscopy. The particle size for all our samples is roughly 5 – 50 μm, and the grain size deduced from the acsence of Scherrer broadening of the hugh-angle X-ray diffraction peaks is > 0.1 μm. The nitrogen occupancy in the bulk materials was quantized by the change of mass after N_2 absorption. Nitrogen occupancy is around 0.94, close to the maximum value of 1. Powder X-ray diffraction (XRD) scans (scanning time > 12 hours) showed a single-phase cubic structure. Magnetization measurements were conducted using a superconducting quantum interference device magnetometer (SQUID, Quantum Design).

Ab-initio calculations based on density functional theory were carried out using norm-conserving pseudopotentials and pseudo-atomic localized basis functions implemented in the OpenMX software package [27]. The generalized gradient approximation (GGA) using PBE theory [28] was used for all the calculations. They were based on a minimal 5 atom basis cell of the cubic structure using 13 × 13 × 13 k-points to evaluate the total energies. Pre-generated fully relativistic pseudopotentials and the pseudo-atomic orbitals with a typical cut-off radius of 6 atomic units (a.u.) were used with $s3p3d3$ for the metal and $s3p3d2$ for the metalloid elements, respectively. A energy cut-off of 300 Ry was used for the numerical integrations. The convergence criterion for the energy minimization procedure was set to 10^{-8} Hartree. In the case of the non-collinear calculations, we show results without spin-orbit interaction (SOI), whose influence on the total energy is negligible (~ 3.5 μeV) compared with the exchange interactions (several meV).

3. Results

3.1. Non-collinear ferrimagnetism in Mn_4N

The origin of the noncollinear ferrimagnetism can be deduced from the magnetic interactions and the crystal structure, identified by X-ray diffraction in Fig. 1c. The lattice parameter $a_0 = 3.865$ Å is also the nearest-neighbour distance between two Mn^{1a} atoms d_{1a1a}. The nearest-neighbour distances between Mn^{3c} and Mn^{1a} or Mn^{3c} d_{1a3c} and d_{3c3c} are both equal to $a_0/\sqrt{2} = 2.733$ Å. Generally, Mn atoms separated by 2.5-2.8 Å have delocalized electrons and couple antiferromagnetically while Mn atoms with longer separations (> 2.9 Å) couple ferromagnetically. Therefore, the Mn^{1a} moments are expected to couple parallel to each other, whereas the small d_{1a3c} distance favors antiparallel coupling between the sublattices. The separation of nearest-neighbor Mn^{3c} atoms d_{3c3c} is responsible for the noncollinear triangular antiferromagnetism of the $3c$ sublattice. Together, these interactions lead to the umbrella-like spin structure, and the overall 120° triangular ferrimagnetism.

Mn_4N has a high Curie temperature T_C (780 K) and a small net saturation moment $m_{tot} = 1.1$ μ_B/f.u. along a [111] direction, as shown in Fig. 2a. The measured moment m_{tot} is the difference of the m_{1a} and three times the ferrimagnetic component of Mn^{3c} m_c^{FiM}, which are 3.8 μ_B and 0.9 μ_B per Mn, respectively [13]. It should be noted that the net moment in Fig. 2a remains constant below 50 K and then drops with increasing temperature. By 160 K ($T/T_C = 0.2$), the moment has fallen by 13% of the 4 K value, in agreement with literature [18]. This temperature-dependence is quite unusual, because according to the collinear mean-field model, the decrease at $T/T_C = 0.2$ should be smaller than 1% (see Fig. 1e-1g) when there is no compensation. The inability to fit a Q-type curve to a collinear mean-field model for Mn_4N [19] is a strong indication of the noncollinear nature of the magnetic order.

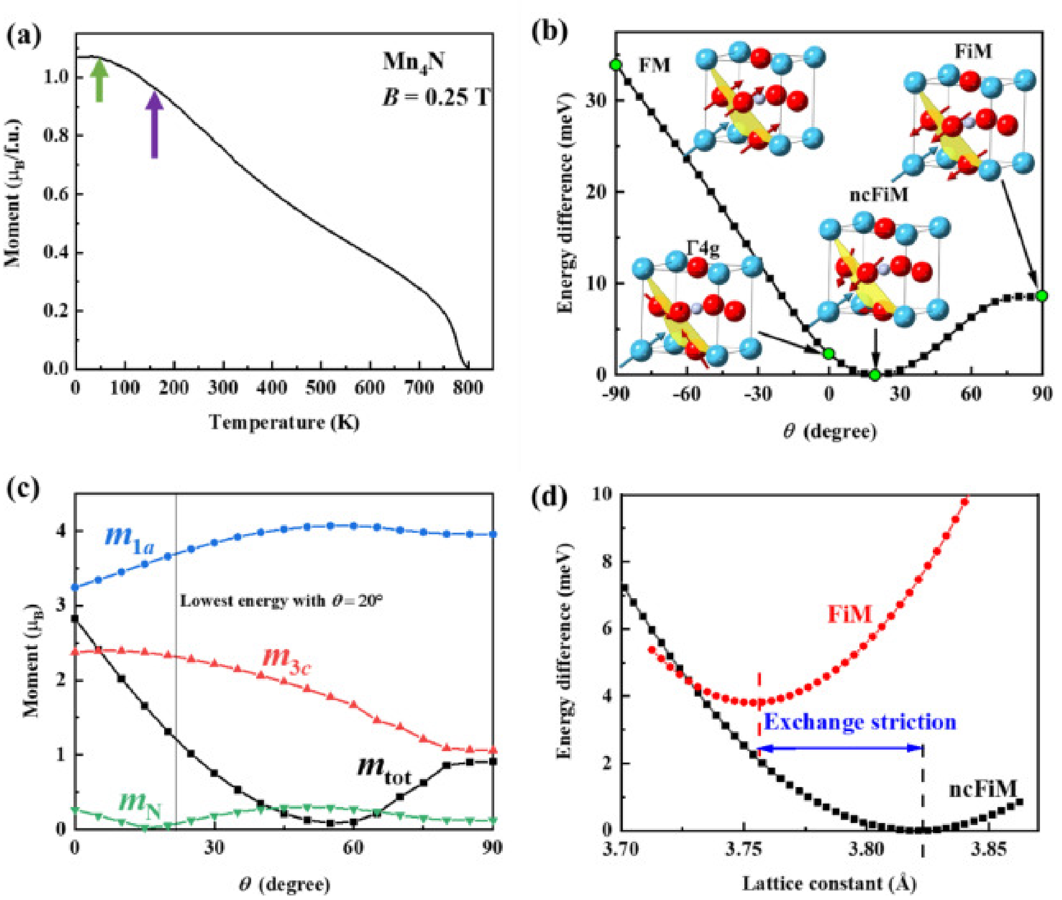

Fig. 2. Noncollinear magnetic structure of Mn_4N. (a) Temperature-dependent magnetization $M(T)$ for Mn_4N. The magnetization remains constant up to 50 K (green arrow) but then drops sharply. At 160 K (purple arrow) the moment has already fallen to 87% of the base temperature value. (b) Energy difference in the calculated magnetic structure as a function of tilt angle θ between m_{3c} and the (111) plane. (c) Magnetic moments as a function of tilt angle θ. (d) Comparison of calculated total energies as a function of lattice constant for the collinear and noncollinear ferrimagnetic structures. (For interpretation of the references to colour in this figure legend, the reader is referred to the web version of this article.)

The noncollinear spin structure is analysed further using a constrained DFT approach, where the directions of the individual spins are pinned to a selected angle but the magnitudes of the moments are allowed to vary freely in the total energy minimization process. The direction of Mn^{1a} is pinned to the body diagonal [111] and the tilt angle θ of the spins the Mn^{3c} atoms is varied (also see inset of Fig. 5b). As the angle is rotated from the collinear ferrimagnetic configuration ($\theta = 90°$) into the (111) plane ($\theta = 0°$, Γ^{4g} spin structure) and then towards a ferromagnetic configuration at $\theta = -90°$ the energy and magnetic moments vary as shown in Fig. 2b and 2c. One can visualize this angle change like a closed umbrella (FiM) that opens out to close to 0° in regular usage, but well beyond it on a windy day (FM, $\theta = -90°$). The relative total energy change of the constrained angle approach is shown Fig. 2b. Following the total energy minimum curve from right to left, we witness a decrease in total energy E_{tot} as the Mn^{3c} moments cant away from the antiparallel spin arrangement towards the (111) plane. The minimum of E_{tot} is found at around $\theta = 20°$. The E_{tot} difference between the collinear ferrimagnetic and noncollinear ferrimagnetic ground state is significant, about 8.5 meV/atom. The calculations also confirm that the FM arrangement ($\theta = -90°$) of the spins on Mn is very unfavourable with an energy difference ~32 meV/atom. Our results indicate that the Mn^{3c} sublattice moments make an angle close to 70° with the Mn^{1a} moments, very far from the simplified picture of collinear ferrimagnetism that is often assumed. Further analysis in Fig. 2c shows the calculated site-specific magnetic moments together with the total magnetic moment per formula unit in our range of interest (θ = 0 to 90°). A strong dependence of magnetization for both magnetic sites as a function of θ is revealed; the Mn^{1a} moment remains ~4 μ_B down to about $\theta = 45°$ and then a significant reduction to ~3.2 μ_B occurs as the Mn^{3c} moments close towards the (111) plane ($\theta = 0°$).

In contrast, the Mn^{3c} moment increases from about 1.1 μ_B up to 2.4 μ_B when the angle closes from collinear FiM towards the Γ^{4g}-like configuration. The E_{tot} minimum suggest magnetic ground-state values of $m_{1a} = 3.65\ \mu_B$, $m_{3c} = 2.35\ \mu_B$ with $m_{tot} = 1.24\ \mu_B$/f.u. Indeed, the collinear ferrimagnetic spin configuration also yields a value of m_{tot} that is close to the experimental one, but we have relaxed both spin configuration for the equilibrium lattice parameters from DFT and find a value $a_0 = 3.75$ Å for the collinear ferrimagnetic state that is smaller than that for the non-collinear ferrimagnetic state $a_0 = 3.82$ Å, in Fig. 2d, which is closer to the experimental value of 3.865 Å at 300K. An earlier calculation [14] found a greater tilt angle and a smaller 3*c* moment, fixing the lattice parameter and exploring a smaller range of θ. The energy difference can be ascribed to the electronic pressure caused by the altered magnetic spin configuration. This exchange striction, like that in FeRh [29], explains the significantly expanded lattice constant for Mn_4N (3.86 Å) compared to its ferromagnetic cousins such as Fe_4N (3.79 Å), Co_4N (3.75 Å) and Ni_4N (3.72 Å) on the one hand and on the other hand it is also manifest throughout the rotation of the spins that alters exchange-split band energies by Coulomb repulsion. This non-Heisenberg like behaviour relates to the spin split *d*-bands crossing the Fermi level that influences the band filling and calculated magnetic moments.

3.2. Doping for compensation

In order to achieve compensation, namely to change the temperature-dependent magnetization from *Q*-type to *N*-type, the main exchange should change from n_{1a3c} to n_{3c3c}, while the 1*a* site moment m_{1a} should be larger than three times the axial component of the 3*c* site moments $3m_{3c}^{FiM}$. This means that Mn on the 1*a* site should be substituted at the appropriate level $x < 1$ in $Mn_{4-x}Z_xN$ for a particular Z. Fig. 3a shows the XRD pattern of $Mn_{3.76}Ga_{0.24}N$, and the low-angle data are expanded in Fig. 3b. The larger intensity of the (110) superlattice peak indicates that $Mn_{3.76}Ga_{0.24}N$ crystallizes in a well-ordered structure with Ga atoms occupying the 1*a* site. This result agrees with previous study that Cr prefers 3*c* site; Fe has no site preference; Co partly prefers 1*a* sites and all elements after Ni strongly prefer the 1*a* site [20,24]. Nonmagnetic Ga weakens the exchange energy density leading to a decreased $T_C = 610$ K. The net moment of 0.17 μ_B/f.u. at 4 K indicates that each Ga decreases the net moment by ~3.8 μ_B, matching both the moment of m_{1a} from neutron diffraction [13] and our calculation. The compensation temperature is then $T_{comp} = 408$ K. In this case, the 1*a* sublattice dominates the magnetization at low temperatures, while the 3*c* sublattice is dominant above compensation. The *M*-*H* curves shown in Fig. 3c exhibit very little hysteresis, indicating weak cubic magnetocrystalline anisotropy. Note the magnetization at 4 K is not saturated even in 5 T (Fig. 3c), further supporting the non-collinear ferrimagnetic structure where the tilt angle θ changes with magnetic field [30].

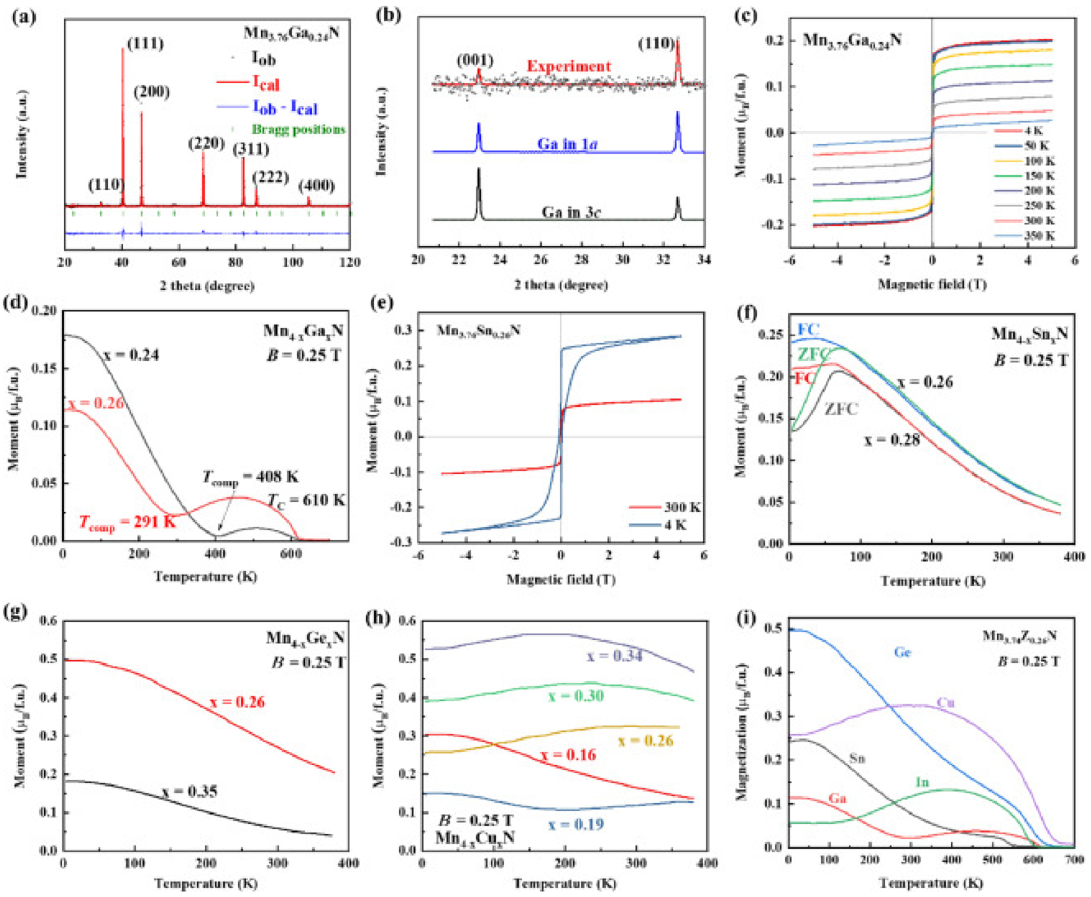

Fig. 3. (a) XRD pattern of $Mn_{3.76}Ga_{0.24}N$. (b) Expanded low-angle data with simulations showing the superlattice peak for $Mn_{3.76}Ga_{0.24}N$. The experimental data confirm that Ga atoms occupy the 1*a* site. (c) Magnetization curves for $Mn_{3.76}Ga_{0.24}N$ at different temperatures. (d) Thermomagnetic scans $Mn_{4-x}Ga_xN$ (x = 0.24 and 0.26). (e) Magnetization curve for $Mn_{3.74}Sn_{0.26}N$ at 4 K and 300 K. (f) Zero-field-cooled (ZFC) and field-cooled (FC) thermomagnetic scans for $Mn_{4-x}Sn_xN$. (g) Thermomagnetic scans for $Mn_{4-x}Ge_xN$ (x = 0.26 and 0.35). (h) Thermomagnetic scans for $Mn_{4-x}Cu_xN$ (x = 0.16 to 0.34). (i) Thermomagnetic scans for $Mn_{3.74}Z_{0.26}N$ (Z = Cu, Ga, Ge, In and Sn). In these figures, *M*-*T* curves without special notes are obtained after FC.

The doping efficiency of different elements from Cu to Sn is shown in Figs. 3e-3i. Unlike Ga, which changes the net moment at the rate of ~3.8 μ_B/atom, the rates for the other elements are significantly different. For Sn with $x = 0.26$, the magnetization is reduced to 0.26 μ_B/f.u., more than 0.12 μ_B/f.u. for Ga with the same *x*. The magnetization curve shows a large hysteresis at 4 K in Fig. 3e, attributed to the first-order transition from antiferromagnetism at low field to ferrimagnetism at high-field, similar to $Mn_{3.2}Sn_{0.8}N$ and $Mn_{3.5}Ni_{0.5}N$ [31]. There is a difference in the *M*-*T* curves measured after field-cooling (FC) and zero-field-cooling (ZFC) shown in Fig. 3f, which is also observed in the In-doped sample ($x = 0.26$). The magnetization is less sensitive to *x* for Sn than for Ga, and this trend towards low doping efficiency is more significant for Ge than Sn, as shown in Fig. 3g. Compensation was not observed below 400 K for Ge with $x = 0.35$. On the other hand, $Mn_{4-x}Cu_xN$ is very sensitive to the compositional changes. The *M*-*T* curve gradually changes from Q-type to *N*-type and finally to *P*-type within a narrow range of *x*, as illustrated in Fig. 3h. The *M*-*T* curves for Cu, Ga, Ge, In and Sn with x = 0.26 are all compared in Fig. 3i). The Cu-doped sample has the highest doping efficiency with a *P*-type *M*-*T* curve without compensation ($T_{comp} < 0$ K). In, Ga doped samples exhibit T_{comp} of 70 K and 291 K respectively with *N*-type *M*-*T* curves. Sn and Ge lead to Q-type *M*-*T* curves without compensation.

We plot data for different compositions of $Mn_{4-x}Z_xN$ at 4 K in Fig. 4a) including both our own data and previous reports [26,[32], [33], [34]. The slope changes significantly from Ni (-6.20 μ_B/atom), Cu (-5.01 μ_B/atom), Zn (-4.35 μ_B/atom), Ga (-3.70 μ_B/atom) to Ge (-2.52 μ_B/atom) with increasing valence electron count for dopants in the fourth period. A similar trend is also found for dopants in the fifth period: Ag (-7.70 μ_B/atom), In (-4.35 μ_B/atom) and Sn (-3.08 μ_B/atom). Based on this trend, the magnetic diagrams for different types of *M-T* curve are shown in the maps of Figs. 4c and 4d. With a small concentrations of dopants, the interaction between 1*a* and 3*c* sites dominates and there is no compensation below the Curie temperature leading to a *Q*-type *M-T* curve. With suitable *x*, the moment if the 1*a* sublattice is still larger than that of the 3*c* sublattice at low temperature, while at high temperature the 3*c* sublattice wins above compensation. Therefore, an *N*-type *M-T* curve is found. When heavily-doped, the 3*c* sublattice dominates throughout whole temperature range, and there is a *P*-type *M-T* curve with no compensation. Elements from the fifth period have a greater ability to compensate than those from the fourth period, and the magnetization is very sensitive to *x*. Therefore, the boundary for different *M-T* curves are shifted to the left (lower *x*) and the useful *N*-type region is narrower.

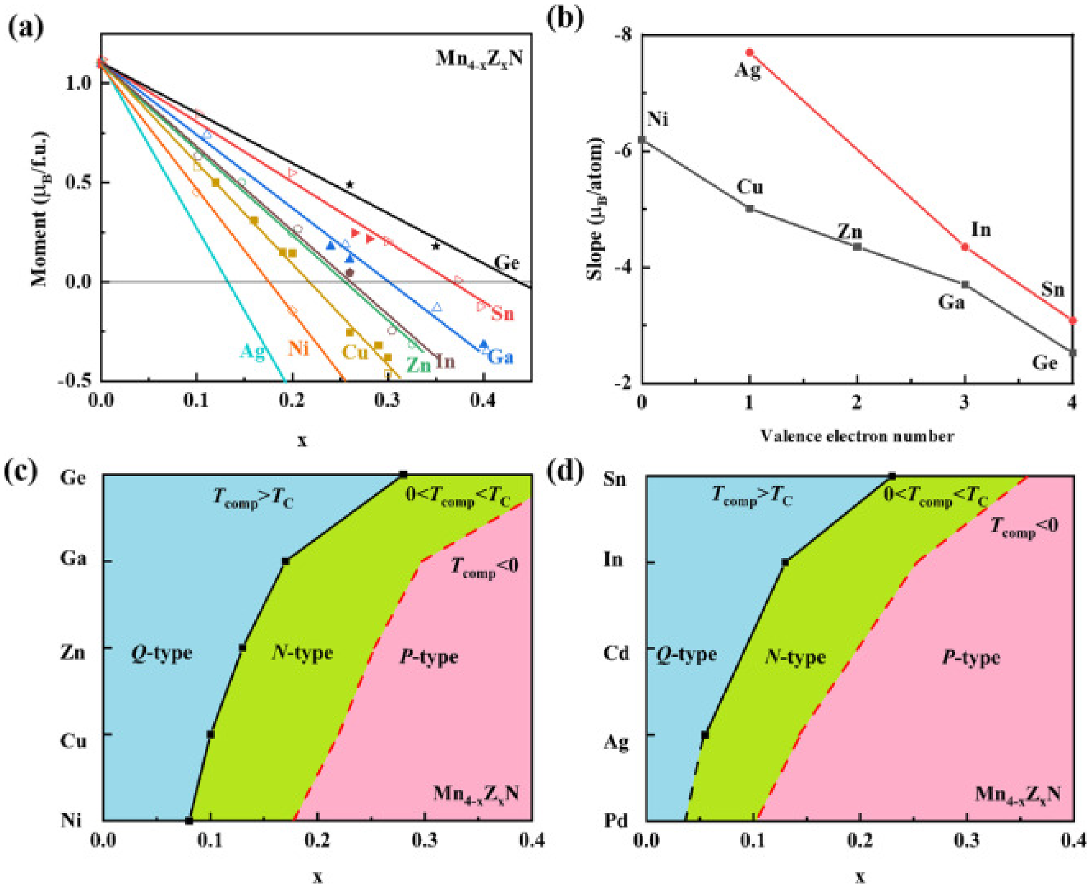

Fig. 4. (a) Summary of the net moment as a function of composition x in $Mn_{4-x}Z_xN$. We include our own data (solid points) and previous reports (open points). (b) The slope in (a) showing different efficiencies. Magnetic diagram for Q, *N* and *P* type *M-T* curves, depending both on x and Z for elements from the fourth (c) and fifth (d) periods.

4. Discussion

The efficiency of the dopants to compensate is analyzed from the view point of lattice constant, magnetic moment, and noncollinear angle from both experimental and theoretical points of view.

4.1. Lattice constant

Compounds with the same *x* but different Z from the same group have the same valance electron number, and the main difference in their effects on the magnetic structure is related to the lattice parameter. Fig. 5a shows a_0 for $Mn_{4-x}Z_xN$ (Z = Cu, Ga, Ge, Ag, Sn In). It is clear that Ag [35], In and Sn [26] lead to a greater increase in lattice parameter than Cu, Ga and Ge for the same *x*, because of their larger atomic radii. The increased lattice parameter translates to a larger atomic separation in the cubic crystal, leading to reduced *p*-*d* hybridisation of Mn^{3c} and increased Mn-Mn exchange that produce a relative increase of magnetism of the 3*c* sublattice. The Mn^{3c} moment is larger and more localized, leading to improved doping efficiency for dopants from the 5th period.

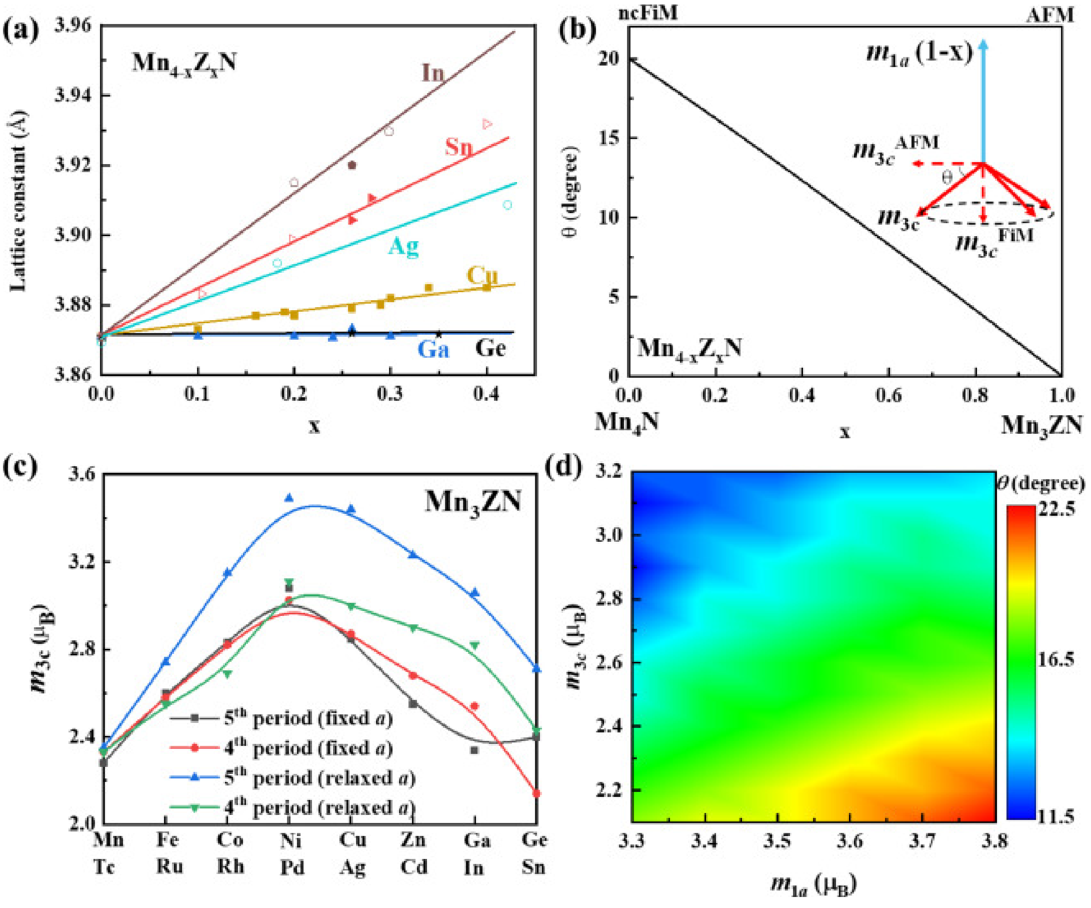

Fig. 5. (a) Lattice parameters for $Mn_{4-x}Z_xN$ (Z = Cu, Ga, Ge, Ag, Sn In), comparing our data (solid points) and previous reports (open points) [26,35]. (b) Calculated tilt angle θ versus x from Eq. 6. (c) Calculated magnetic moments for Mn^{3c} in Mn_3ZN ($x = 1$). (d) Tilt angle θ for different m_{1a} and m_{3c} deduced from DFT.

4.2. Magnetic moment

Since the nearest-neighbor of Mn^{1a} is always Mn^{3c}, the direct magnetic coupling between Mn^{1a} atoms is weak. As a result, the moment for the Mn^{1a} is not influenced significantly by doping, as also indicated from neutron diffraction [36]. Therefore the effect of doping on the net magnetization comes mainly from Mn^{3c}. We built our DFT model to capture trends in the electronic and magnetic structures and used the simplest 5-atom unit cell to model our experimental observations with different compositions. This model allows us to compare trends for the metallic perovskite with $x = 1$, when the 3*c* site is fully occupied by Mn and the symmetry is cubic.

The calculated Mn^{3c} moment as a function of valence electron count in Mn_3ZN from Mn to Ge in the 4th period and from Tc to Sn in 5th period is plotted in Fig. 5c. The magnetic behaviour shows the same trend; an initial increase saturates around Ni and Pd, and drops monotonically afterwards. In order to separate the electronic effects from the impact of chemical pressure on the lattice parameter, we first fixed a_0 of all members of the series to that of Mn_4N (3.82 Å). This is shown by the solid red and black lines for the 4th and 5th periods in Fig. 5c. The peak at Ni, which has three electrons more than Mn, indicates localized moment behaviour with striking similarities with the Slater-Pauling rule. These three extra electrons are shared by the three nearby Mn^{3c} atoms, and hence each of the Mn^{3c} atoms get one more electron, becoming like iron, which shows the largest average moment in 3*d* alloys. The influence of the lattice constant on the moment expected on Mn^{3c} without constraint is also drawn in green and blue lines (Fig. 5c) for comparison. The same trend is maintained, with peaks at Z = Ni and Pd. The main difference is found on the right hand side of the curves, especially for elements from the 5th period, as it relates to the expanded lattice parameters with additional valence electrons compared to the Z = Mn reference. The significant change in the amplitude of m_{3c} is one of the main reasons for the different doping efficiencies. In addition, the orientation of m_{3c} also depends on its amplitude that further impacts the efficiency of compensation as we discuss in the following section.

4.3. Tilt angle

Two questions concerning the tilt angle θ between $\boldsymbol{m}_{3c}$ and the (111) plane are: How does θ change with x, and with the different dopings?

The 3c moment has two components, one component $m_{3c}{}^{\mathrm{Fi}}$ along the ferrimagnetic [111] axis and the other $m_{3c}{}^{\mathrm{AFM}}$ in triangular antiferromagnetic (111) plane. The molecular field acting on 3c site also has two components, parallel and perpendicular to the [111] axis H^{Fi} and H^{AFM}, corresponding to the ferrimagnetism and in-plane antiferromagnetism. They satisfy the relationships

$$H^{AFM} = -2n_{3c3c}m_{3c}\cos\theta\cos 120^{\circ} \tag{1}$$

$$H^{FiM} = n_{1a3c}m_{1a}\,(1-x) - 2n_{3c3c}m_{3c}sin\theta \tag{2}$$

$$m_{3c}^{Fi} = m_{3c}sin\theta \tag{3}$$

$$m_{3c}^{AFM} = m_{3c}cos\theta \tag{4}$$

$$tan\theta = H^{FiM}/H^{AFM} \tag{5}$$

where n_{3c3c} and n_{1a3c} are the Weiss coefficients for interactions between 3c-3c Mn and 1a-3c Mn, as shown from the inset of Fig. 5b. In Eqs. 1 and 2, the in-plane antiferromagnetism considers the interaction from the other two nearest neighbor Mn^{3c} in the 120° triangular spin structure; the negative sign of m_{3c} is already considered. Substituting Eqs. 1 and 2 into Eq. 5, we get

$$sin\theta = n_{1a3c}m_{1a}\,(1-x)\,/\,(3n_{3c3c}m_{3c}) \tag{6}$$

Originally θ was estimated from neutron diffraction to be about 70° (nearly collinear), with $m_{3c}{}^{\mathrm{Fi}} = 0.9\ \mu_B$, $m_{3c}{}^{\mathrm{AFM}} = 0.36\ \mu_B$, $m_{3c}= 0.97\ \mu_B$, $m_{1a}= 3.8\ \mu_B$ but with large error bars [13]. This means the doping efficiency should be weaker than –(3.8+0.36) = -4.16 μ_B/atom, if we assume that the magnetic structure becomes collinear ferrimagnetic after doping. But from both our and previous experiments, doping Ni, Ag, Cu is much more effective, indicating that $m_{3c}{}^{\mathrm{AFM}}$ was underestimated. This is also found in our DFT calculations, where θ = 20° for binary $\mathrm{Mn_4N}$. Thus when we plot the relationship between x and θ in Eq. 6 (Fig. 5b), we find that θ decreases almost linearly with x. The umbrella-like triangular spin structure of Mn^{3c} rotates away from the [111] direction and becomes in-plane and therefore the net moment changes at a slower rate, as confirmed by a comparative neutron study of $\mathrm{Mn_{3.2}Ga_{0.8}N}$ and $\mathrm{Mn_4N}$ [36]. Finally, when x = 1, Mn^{1a} is completely replaced by the nonmagnetic dopant and $\mathrm{Mn_3ZN}$ is a 120 ° triangular topological antiferromagnet in the (111) plane provided the crystal remains cubic.

When doped with different elements from Cu to Ge, or from Ag to Sn, the decrease of m_{3c} with increase of valance electrons leads to a rise of θ according to Eq. 6. This can weaken the effect of decreasing $m_{3c}{}^{\mathrm{Fi}}$ according to Eq. 3. Similarly, considering the increased lattice constant for dopants from the 5th period, the enhanced m_{3c} can also lead to a drop of θ, weakening the influence on $m_{3c}{}^{\mathrm{Fi}}$. We further estimate θ by DFT calculation based on different m_{1a} and m_{3c} manganese site moments, as shown in Fig. 5d. We use the fixed spin moment (FSM) approach, where the amplitude of the magnetic moments on both sites is fixed. In Fig 5d, we plot the angles for minimum total energy $E_{\mathrm{tot}}(m_{1a}, m_{3c})$. The general trend is that the larger m_{3c} for a given m_{1a}, the smaller θ. The larger m_{3c} moment tends to stay in the (111) plane, and only the increasing moment on the 1a site could compensate for this rotation. This is in qualitative agreement with Eq. 6 and the vanishing moment on m_{1a} with increasing x, from experiment.

4.4. Best dopant for compensated ferrimagnetism

$Mn_{4-x}Z_xN$ thin films are already attracting increasing attention for spintronics [37,38]. Most studies have been done with Ni or Co [22], [23], [24], [25], but they are not ideal for achieving compensation. Beside the demand for compensation, additional requirements must be considered when choosing the best dopants. Based on our analysis, Ga appears to be the most suitable dopant in $Mn_{4-x}Z_xN$ films for the following reasons: First, earlier elements from 4th period like Ni compensate the moment with small values of x. As the total moment is very sensitive to the composition, it is difficult to control the composition precisely and homogeneously. Second, for elements that have many additional valance electrons like Ge, a large value of x is needed due to the low doping efficiency. As a result, the Curie temperature drops substantially, which is not beneficial for room-temperature applications. Third, Ga does not significantly increase the lattice constant compared to elements from 5th period so that a series of thin films can be grown with different compositions x and a similar tetragonal distortion is expected on the same substrate. The slight tetragonal distortion ($c/a \sim 0.99$) due to biaxial strain imposed at the interface of the film and substrate is the origin of perpendicular [001] anisotropy. A smaller lattice constant of the film than that of common substrates, such as $SrTiO_3$ with $a_{001} = 3.91$ Å, is the key for the in-plane tensile strain and perpendicular anisotropy [39,40], which can be easily realized in Ga-doped samples. Finally, the doping efficiency of Ga, -3.70 μ_B/atom coincides with m_{1a}. This is a consequence of a combination of an increased m_{3c} and a decreased θ rather than simply the nonmagnetic nature of the dopant.

5. Conclusion

From our experimental and theoretical study of the rare-earth-free noncollinear ferrimagnetic metals $Mn_{4-x}Z_xN$, we conclude that the noncollinear triangular ferrimagnetism originates from the structure of the Mn^{3c} (111) kagome planes with a small Mn-Mn interatomic separation that leads to frustration of the antiferromagnetic nearest-neighbor interactions. The tilt angle of the moments from the (111) planes, $\theta = 20°$, is smaller than previously thought. There is a wide choice of substitutions to achieve magnetic compensation at room temperature. The efficiency of different elements in this respect drops gradually with increasing valance electron count from group 11 (Cu, Ag) to group 14 (Ge, Sn). The Mn^{1a} moment is not sensitive to the dopants, while the Mn^{3c} moment peaks at Ni or Pd and then drops with further valance electron addition. The higher efficiency of elements from 5th period is due to the larger lattice constant, which weakens the hybridization of Mn^{3c} and N and leads to an increase of m_{3c}. In addition, the tilt angle decreases with increasing m_{3c} and composition x. Based on the above results, Ga is the recommended dopant for $Mn_{4-x}Z_xN$ for thin film spintronics with perpendicular anisotropy.

Declaration of Competing Interest

The authors declare that they have no known competing financial interests or personal relationships that could have appeared to influence the work reported in this paper.

Acknowledgement

Yangkun He and Rui Zhang contribute equally to the work. We thank Yu Kang for high-temperature measurements. This work was supported by Science Foundation Ireland, under the MANIAC, SFI-NSF China project (17/NSFC/5294) and ZEMS project 16/IA/4534.

Recommended articles

References

[1] T. Jungwirth, X. Marti, P. Wadley, J. Wunderlich
Antiferromagnetic spintronics
Nat. Nanotech., 11 (2016), pp. 231-241
CrossRef Google Scholar

[2] S. Nakatsuji, N. Kiyohara, T. Higo
Large anomalous Hall effect in a non-collinear antiferromagnet at room temperature

Nature, 527 (2015), pp. 212-215
CrossRef Google Scholar

[3] A.K. Nayak, J.E. Fischer, Y. Sun, B. Yan, J. Karel, A.C. Komarek, C. Shekhar, N. Kumar, W. Schnelle, J. Kübler, C. Felser, S.S.P. Parkin
Large anomalous Hall effect driven by a nonvanishing Berry curvature in the noncolinear antiferromagnet Mn_3Ge
Sci. Adv., 2 (2016), Article e1501870
View Record in Scopus Google Scholar

[4] S.K. Kim, G.S.D. Beach, K.J. Lee, T. Ono, T. Rasing, H. Yang
Ferrimagnetic spintronics
Nat. Mater., 21 (2022), pp. 24-34
CrossRef Google Scholar

[5] H.A. Zhou, T. Xu, H. Bai, W. Jiang
Efficient Spintronics with Fully Compensated Ferrimagnets
J. Phys. Soc. Japan, 90 (2021), Article 081006
CrossRef View Record in Scopus Google Scholar

[6] J.M.D. Coey
Magnetism and Magnetic Materials
Cambridge Univ. Press, Cambridge (2010)
Google Scholar

[7] M.K. Wilkinson, N.S. Gingrich, C.G. Shull
The magnetic structure of Mn_2Sb
J. Phys. Chem. Solids, 2 (1957), pp. 289-300
Article Download PDF View Record in Scopus Google Scholar

[8] O.S. Volkova, V.V. Mazurenko, I.V. Solovyev, E.B. Deeva, I.V. Morozov, J.-Y. Lin, C.K. Wen, J.M. Chen, M. Abdel-Hafiez, A.N. Vasiliev
Noncollinear ferrimagnetic ground state in $Ni(NO_3)_2$
Phys. Rev. B, 90 (2014), Article 134407
CrossRef View Record in Scopus Google Scholar

[9] R.N. Bhowmik, R. Ranganathan, R. Nagarajan
Lattice expansion and noncollinear to collinear ferrimagnetic order in a $MnCr_2O_4$ nanoparticle
Phys. Rev. B, 73 (2006), Article 144413
CrossRef View Record in Scopus Google Scholar

[10] P. Wolfers, S. Miraglia, D. Fruchart, S. Hirosawa, M. Sagawa, J. Bartolome, J. Pannetier
Low temperature crystal and magnetic structures of $Ho_2Fe_{14}B$
J. Less-common Met., 162 (1990), pp. 237-249
Article Download PDF View Record in Scopus Google Scholar

[11] W.J. Takei, G. Shirane, B.C. Frazer
Magnetic Structure of Mn_4N
Phys. Rev., 119 (1960), p. 122
View Record in Scopus Google Scholar

[12] W.J. Takei, R.R. Heikes, G. Shirane
Magnetic Structure of Mn_4N-Type Compounds
Phys. Rev., 125 (1962), p. 1893
View Record in Scopus Google Scholar

[13] D. Fruchart, D. Givord, P. Convert, P. l'Heritier, J.P. Senateur
The non-collinear component in the magnetic structure of Mn_4N
J. Phys. F: Metal Phys., 9 (1979), p. 2431
CrossRef View Record in Scopus Google Scholar

[14] M. Uhl, S.F. Matar, P. Mohn
Ab initio analysis of magnetic properties in noncollinearly ordered Mn_4N
Phys. Rev. B, 55 (1997), p. 2995
View Record in Scopus Google Scholar

[15] V.T.N. Huyen, M-T. Suzuki, K. Yamauchi, T. Oguchi
Topology analysis for anomalous Hall effect in the noncollinear antiferromagnetic states of Mn_3AN (A = Ni, Cu, Zn, Ga, Ge, Pd, In, Sn, Ir, Pt)
Phys. Rev. B, 100 (2019), Article 094426
View Record in Scopus Google Scholar

[16] T. Bayaraa, C. Xu, L. Bellaiche
Magnetization Compensation Temperature and Frustration-Induced Topological Defects in Ferrimagnetic Antiperovskite Mn_4N
Phys. Rev. Lett., 127 (2021), Article 217204
View Record in Scopus Google Scholar

[17] S. Chikazumi
Physics of ferromagnetism
Oxford University Press (1997)
Google Scholar

[18] C. Li, Y. Yang, L. Lv, H. Huang, Z. Wang, S. Yang
Fabrication and magnetic characteristic of ferrimagnetic bulk Mn_4N
J. Alloys and Compd., 457 (2008), pp. 57-60
Article Download PDF Google Scholar

[19] M. Mekata, J. Haruna, H. Takaki
Localized Magnetic Moments in Mn_4N
J. Phys. Soc. Jpn., 21 (1966), pp. 2267-2273
View Record in Scopus Google Scholar

[20] R. Niewa
Metal-Rich Ternary Perovskite Nitrides
Eur. J. Inorg. Chem., 2019 (2019), pp. 3647-3660
CrossRef View Record in Scopus Google Scholar

[21] J.C. Lin, P. Tong, W. Tong, Y.M. Zouc, C. Yang, F. Zhu, X.K. Zhang, L.F. Li, M. Wang, Y. Wu, S. Lin, W.H. Song, X.B. Zhu, Y.P. Sun
Large and constant coefficient of negative thermal expansion covering a wide temperature range in $Zn_{1-x}Mn_xNMn_3$ ($0 \le x \le 0.3$)
Scr. Mater., 152 (2018), pp. 6-10
Article Download PDF View Record in Scopus Google Scholar

[22] S. Ghosh, T. Komori, A. Hallal, J.P. Garcia, T. Gushi, T. Hirose, H. Mitarai, H. Okuno, J. Vogel, M. Chshiev, J. Attané, L. Vila, T. Suemasu, S. Pizzini
Current-Driven Domain Wall Dynamics in Ferrimagnetic Nickel-Doped Mn4N Films: Very Large Domain Wall Velocities and Reversal of Motion Direction across the Magnetic Compensation Point
Nano Lett, 21 (2021), pp. 2580-2587
CrossRef View Record in Scopus Google Scholar

[23] T. Komori, T. Gushi, A. Anzai, L. Vila, J. Attané, S. Pizzini, J. Vogel, S. Isogami, K. Toko, T. Suemasu
Magnetic and magneto-transport properties of Mn_4N thin films by Ni substitution and their possibility of magnetic compensation
J. Appl. Phys., 125 (2019), Article 213902
CrossRef View Record in Scopus Google Scholar

[24] K. Ito, Y. Yasutomi, S. Zhu, M. Nurmamat, M. Tahara, K. Toko, R. Akiyama, Y. Takeda, Y. Saitoh, T. Oguchi, A. Kimura, T. Suemasu
Manipulation of saturation magnetization and perpendicular magnetic anisotropy in epitaxial $Co_xMn_{4-x}N$ films with ferrimagnetic compensation
Phys. Rev. B, 101 (2020), Article 104401
View Record in Scopus Google Scholar

[25] H. Mitarai, T. Komori, T. Hirose, K. Ito, S. Ghosh, S. Honda, K. Toko, L. Vila, J. Attané, K. Amemiya, T. Suemasu
Magnetic compensation at two different composition ratios in rare-earth-free $Mn_{4-x}Co_xN$ ferrimagnetic films
Phys. Rev. Materials, 4 (2020), Article 094401
View Record in Scopus Google Scholar

[26] M. Mekata
Magnetic study on Mn_4N and its related compounds
J. Phys. Soc. Japan, 17 (1962), pp. 796-803
View Record in Scopus Google Scholar

[27] See http://www.openmx-square.org. 2022
Google Scholar

[28] J.P. Perdew, K. Burke, M. Ernzerhof
Generalized Gradient Approximation Made Simple
Phys. Rev. Lett., 77 (1996), p. 3865
Google Scholar

[29] U. Aschauer, R. Braddell, S.A. Brechbuh, P.M. Derlet, N.A. Spaldin
Strain-induced structural instability in FeRh
Phys. Rev. B, 94 (2016), Article 014109
CrossRef View Record in Scopus Google Scholar

[30] P.A. Dickof, P.J. Schurer, A.H. Morrish
Magnetic structure of zinc-substituted magnetite at T =4.2 K
Phys. Rev. B, 22 (1980), p. 115
View Record in Scopus Google Scholar

[31] D. Boldrin, L.F. Cohen
The role of competing magnetic interactions on the abnormal expansion properties in manganese antiperovskites, $Mn_{3+x}A_{1-x}N$ (A = Ni, Sn)
J. Alloys and Compd., 699 (2017), pp. 887-891
Article Download PDF View Record in Scopus Google Scholar

[32] M.R. Fruchart, J.P. Bouchaud, M.E. Fruchart, M.G. Lorthioir, R. Madar, A. Rouault
Sur les transitions magnetiques du premier ordre dans les perowskites metalliques du manganese
Mat. Res. Bull, 2 (1967), pp. 1009-1020
Article Download PDF View Record in Scopus Google Scholar

[33] W.J. Feng, D. Li, Q. Zhang, Y.F. Deng, S. Ma, Z.D. Zhang
Structure, magnetic and electrical transport properties of $Mn_{4-x}Ag_xN$ compounds
Mater. Sci. (Poland), 27 (2009), p. 33

View Record in Scopus Google Scholar

[34] R. Madar
Thesis, University of Paris, N° 686
Centre de Documentation du CNRS, Paris (1970)
Google Scholar

[35] N.P. Lu, T. Xu, Z.X. Cao, A.L. Ji
Ternary $Mn_3NMn_{1-x}Ag_x$ compound films of nearly constant electrical resistivity and their magnetic transport behaviour
J. Phys. D: Appl. Phys., 49 (2016), Article 045308
CrossRef Google Scholar

[36] D. Fruchart, R.Fruchart Ph.L'Héritier
Transformations de phases dans les nitrures et carbures du manganese de structure-type perovskite
Mat. Res. Bull., 15 (1980), pp. 415-420
Article Download PDF View Record in Scopus Google Scholar

[37] T. Suemasu, L. Vila, J.P. Attané
Present Status of Rare-earth Free Ferrimagnet Mn4N and Future Prospects of Mn_4N-based Compensated Ferrimagnets
J. Phys. Soc. Japan, 90 (2021), Article 081010
CrossRef View Record in Scopus Google Scholar

[38] Z. Zhang, W. Mi
Progress in ferrimagnetic Mn_4N films and its heterostructures for spintronics applications
J. Phys. D: Appl. Phys., 55 (2022), Article 013001
CrossRef Google Scholar

[39] Y. Yasutomi, K. Ito, T. Sanai, K. Toko, T. Suemasu
Perpendicular magnetic anisotropy of Mn_4N films on MgO(001) and $SrTiO_3$(001) substrates
J. Appl. Phys., 115 (2014), p. 17A935
CrossRef View Record in Scopus Google Scholar

[40] T. Hirose, T. Komori, T. Gushi, A. Anzai, K. Toko, T. Suemasu
Strong correlation between uniaxial magnetic anisotropic constant and in-plane tensile strain in Mn_4N epitaxial films
AIP Adv, 10 (2020), Article 025117
CrossRef View Record in Scopus Google Scholar

Cited by (2)

Magnetic structure of 3d-element doped Mn<inf>4</inf>N films confirmed by X-ray magnetic circular dichroism – Conditions for magnetic compensation

2022, Journal of Magnetism and Magnetic Materials

Show abstract

Noncollinear ferrimagnetism and anomalous Hall effects in Mn4 N thin films

2022, Physical Review B